

Multifunctional Gadolinium-Doped Mesoporous TiO₂ Nanobeads: Photoluminescence, Enhanced Spin Relaxation, and Reactive Oxygen Species Photogeneration, Beneficial for Cancer Diagnosis and Treatment

Roghayeh Imani, Ralf Dillert, Detlef W. Bahnemann, Meysam Pazoki, Tomaž Apih, Veno Kononenko, Neža Repar, Veronika Kralj-Iglič, Gerrit Boschloo, Damjana Drobne, Tomas Edvinsson,* and Aleš Iglič*

Materials with controllable multifunctional abilities for optical imaging (OI) and magnetic resonant imaging (MRI) that also can be used in photodynamic therapy are very interesting for future applications. Mesoporous TiO₂ sub-micrometer particles are doped with gadolinium to improve photoluminescence functionality and spin relaxation for MRI, with the added benefit of enhanced generation of reactive oxygen species (ROS). The Gd-doped TiO₂ exhibits red emission at 637 nm that is beneficial for OI and significantly improves MRI relaxation times, with a beneficial decrease in spin–lattice and spin–spin relaxation times. Density functional theory calculations show that Gd³⁺ ions introduce impurity energy levels inside the bandgap of anatase TiO₂, and also create dipoles that are beneficial for charge separation and decreased electron–hole recombination in the doped lattice. The Gd-doped TiO₂ nanobeads (NBs) show enhanced ability for ROS monitored via •OH radical photogeneration, in comparison with undoped TiO₂ nanobeads and TiO₂ P25, for Gd-doping up to 10%. Cellular internalization and biocompatibility of TiO₂@xGd NBs are tested in vitro on MG-63 human osteosarcoma cells, showing full biocompatibility. After photoactivation of the particles, anticancer trace by means of ROS photogeneration is observed just after 3 min irradiation.

Dr. R. Imani, Prof. R. Dillert, Prof. D. W. Bahnemann
Institut fuer Technische Chemie
Gottfried Wilhelm Leibniz Universitaet Hannover
Callinstrasse 3, D-30167 Hannover, Germany

Dr. R. Imani, Prof. G. Boschloo
Department of Chemistry–Physical Chemistry Division
Ångström Laboratory
Uppsala University
Box 523, Lägerhyddsvägen 1, 75120 Uppsala, Sweden

Dr. R. Imani, Prof. A. Iglič
Faculty of Electrical Engineering
Biophysics Laboratory
University of Ljubljana SI-1000, Slovenia
E-mail: ales.iglic@fe.uni-lj.si

DOI: 10.1002/sml.201700349

Prof. R. Dillert
Laboratory of Nano and Quantum Engineering
University of Hannover
Schneiderberg 39, 30167 Hannover, Germany

Prof. D. W. Bahnemann
Laboratory “Photoactive Nanocomposite Materials”
Saint-Petersburg State University
Saint-Petersburg 198504, Russia

Dr. M. Pazoki
Department of Chemistry–Structural Chemistry Division
Ångström Laboratory, Uppsala University
Box 538, Lägerhyddsvägen 1, 75120 Uppsala, Sweden



1. Introduction

In recent years, TiO₂ was regarded as a potential photosensitizer in the field of photodynamic therapy (PDT) due to its high chemical stability, excellent biocompatibility when not irradiated, and photoreactivity.^[1–3] The photocytotoxicity of TiO₂ to malignant cells, based on its reactive oxygen species (ROS) photogeneration ability under UV-A irradiation, was reported by different groups.^[4–9] It has been reported that various ROS, such as superoxide (O₂^{•-}), singlet oxygen (¹O₂), hydroxyl radical ([•]OH), hydroperoxyl radical (HO₂[•]), and hydrogen peroxide (H₂O₂), are generated on the TiO₂ surface upon UV-A irradiation in aqueous solutions.^[10] ROS are capable of destroying bacteria, viruses, and cancer cells, where manipulation of ROS levels with exogenous agents has been reported to be an efficient way to destroy cancer cells,^[11] where the low-lying energy of the photogenerated hole in TiO₂ makes the generation of [•]OH specifically effective. Cancerous cells normally contain an elevated level of ROS and are therefore more sensitive to any further ROS increase.^[11] In the tumor region, externally applied radiation stimulates increased production of ROS by the photosensitizer, which is beneficially used in PDT.^[12] TiO₂ is one of the most efficient of all nanoparticulate systems in performing ROS photogeneration, which is the most important prerequisite for practical application in photodynamic therapy.^[13] TiO₂ itself, however, is not intrinsically suited for imaging purposes, as it has very faint fluorescence for optical imaging (OI), and it has dominant Raman bands in a very low energy region (≈100–300 cm⁻¹); it is not magnetic and it does not have a substantially large atomic number to have a significant contrast in magnetic resonance imaging (MRI) and X-ray measurements.^[2,3,14] Therefore, a current challenge to the use of TiO₂ nanostructures as a photosensitizer is the addition of imaging agents (e.g., contrasts), which have to be incorporated into TiO₂ to ensure reliable tracking of TiO₂ delivery. To avoid damage to normal cells, monitoring and tracking of the TiO₂ localization and concentration in the cell tissues around the cancerous cell before irradiation, as well as during irradiation are vital.^[15–17] The powerful future implementation of TiO₂ in photodynamic therapies is conditional on modification of TiO₂ nanostructures to gain maximum imaging and therapeutic efficacy of TiO₂ nanostructures, a compromise among ROS generation, endocytosis, and low toxicity to nontarget cells and cell imaging properties.^[16]

Among different imaging methods, OI has by far the greatest resolution that can visualize structures on the subcellular scale.^[18–20] MRI has the advantage of being widely used as diagnostic, noninvasive, or minimally invasive tools for imaging.^[21] The combination of MRI and OI in one MRI–OI probe is particularly useful. Combined MRI–OI agents have great application potential in selective tumor labeling for oncological diagnosis and surgery.^[22,23]

Recently, surface labeled TiO₂ nanoparticles, nanotubes, or nanopores with fluorescent dye or magnetic resonance contrast agents have been successfully prepared and utilized for cell imaging through OI or MRI,^[2,3,14] but surface modifications of TiO₂ with organic capping ligands significantly lower the ROS photogeneration activity of TiO₂.^[24] To address this issue, TiO₂ photocatalysts are often produced in the form of a framework that can be calcined at high temperatures, to ensure a clean surface and well developed crystallinity;^[5] therefore, for effective use of TiO₂ in targeted cancer therapy, surface coverage with an imaging agent is not a good solution. For solving this problem, incorporation of imaging elements inside the crystalline structure of TiO₂ could be a better solution. Different elements such as Fe, Co, Ni, etc., could be incorporated into crystalline structure of TiO₂ as a medical imaging agent. In the last few years, lanthanide (which are often collectively known as the rare earth (RE) elements) nanocompounds have attracted considerable attention as medical imaging probes.^[25] Currently, gadolinium (Gd) compounds are used as a commercial MRI contrast agent in hospitals,^[21] as well as luminescent nanomaterials that incorporate RE ions within their structures, and have also gained considerable attention as optical imaging probes in medicine.^[18] Many efforts have been devoted to exploring TiO₂-based phosphors with various morphologies and dopant.^[26–30]

One of the drawbacks of nanomaterials is general nanotoxicity. The optimal “safe” size is based on numerous examples in literature, which show clearly that 100 nm is the distinct cut-off size below which atypical surface reactivity arises and causes normal nanoscale toxicity.^[5,31] Based on this critical feature, recently we have engineered mesoporous TiO₂ nanobeads (TiO₂ NBs) having a size greater than 100 nm, to avoid normal nanotoxicity, and on the other hand keeps the high surface area comparable to nanometer-size particles by utilizing mesoporosity. TiO₂ NBs totally were biocompatible in the absence of irradiation that also

Prof. T. Apih
Jožef Stefan Institute
Jamova 39, SI-1000 Ljubljana, Slovenia
V. Kononenko, N. Repar, Prof. D. Drobne
Biotechnical Faculty
Department of Biology
University of Ljubljana
Večna pot 111, SI-1000 Ljubljana, Slovenia
Prof. V. Kralj-Iglič
Faculty of Health Sciences
Biophysics Laboratory
University of Ljubljana
SI-1000 Ljubljana, Slovenia

Dr. M. Pazoki, Prof. T. Edvinsson
Department of Engineering Sciences–Solid State Physics Division
Uppsala University
Box 534, 75121 Uppsala, Sweden
E-mail: tomas.edvinsson@angstrom.uu.se

possesses a high ability for ROS photogeneration and cancer cell destruction under UV-A irradiation.^[5,32] Here we report doping of TiO₂ NBs with the rare earth element Gd to add multifunctional OI–MRI properties, as well enhanced ROS photogeneration capacity to the TiO₂ NBs.

The photocatalytic activities of the TiO₂@xGd NBs in terms of ROS photogeneration were quantified via •OH radical measurement with fluorescence probe and compared with a standard TiO₂ powder (P25). The details of the bandgap states introduced by the Gd-doping, and the consequences for the photoluminescence (PL) and photocatalytic enhancement are investigated and supported by density functional theory (DFT) calculations. Finally, the MG-63 in vitro cell culture was used to study the internalization potential and cytotoxicity of TiO₂@xGd NBs. We discuss the advantage of TiO₂@xGd NBs for simultaneous imaging and PDT of cancer cells. Data presented here, proving a notable biocompatibility and multifunctionality of TiO₂@xGd NBs for cancer diagnosis and treatment, are very interesting for future applications.

2. Results and Discussion

2.1. Morphological and Structural Description of TiO₂@xGd NBs

The morphological characteristics analyzed by scanning electron microscopy (SEM), transmission electron microscopy (TEM), and elemental composition/distribution by energy-dispersive X-ray spectroscopy (EDS) of TiO₂ NBs, TiO₂@5%Gd NBs, and TiO₂@10%Gd NBs are shown in **Figure 1**, where all three structures consist of submicrometer nanospheres with a rough surface, while a few distinct differences between the Gd-doped TiO₂ NBs and the pure TiO₂ NBs can be observed: i) the average diameter of Gd-doped TiO₂ NBs (≈800 nm) is higher than that of the undoped TiO₂ NBs (≈500 nm), ii) Gd-doped TiO₂ NBs have a smoother surface compared to pure TiO₂ NBs, and iii) nanostar clusters appeared on top of Gd-doped TiO₂ NBs (marked with a red circle in **Figure 1g**). A number of nanostar clusters on TiO₂@10%Gd NBs increased significantly compared to TiO₂@5%Gd NBs, and no trace of nanostar clusters can be seen on TiO₂ NBs surfaces (**Figure 1a,d,g**).^[33] High magnification TEM measurements were conducted to obtain more information about the structural properties of nanostar clusters (**Figure 1j,k**). TEM images indicated the nanostar clusters are composed of two kinds of structures: i) nanocrystals with different shapes and an average size of ≈50 nm, ii) very small, packed semi-crystalline nanoparticles of ≈5 nm in dimension (**Figure S1**, Supporting Information).

A structural transformation was observed in the case of TiO₂ NBs having a high Gd content (exceeding 10%, TiO₂@15%Gd and TiO₂@20%Gd). As is apparent in the SEM images (**Figure S2a,d**, Supporting Information) no spheres were formed in these structures, where TEM analysis showed that TiO₂@15%Gd NBs are composed of very small (≈5 nm) semicrystalline nanoparticles (**Figure S2b**, Supporting Information), while TiO₂@20%Gd NBs are composed of densely

packed crystalline nanoparticles with a visible crystalline plane (**Figure S2e**, Supporting Information). The Gd-doping concentration in the synthesized structures was found by an energy-dispersive X-ray analysis during SEM imaging to be very close to that in the precursor solution (**Figures S3–S7**, Supporting Information).

The X-ray diffraction (XRD) results (**Figure 2a**) confirmed that anatase is the predominant phase for TiO₂ NBs, TiO₂@5%Gd NBs, and TiO₂@10%Gd NBs and all (101), (004), (200), (105), (211), (213), (204) peaks observed in the XRD patterns are related to the anatase phase of TiO₂ (JCPDS number: 21-1272).^[34,35] However, the crystallinity was reduced by increasing the Gd amount, in agreement with previous observations.^[35] The relative crystallite sizes of the structures were calculated with the Debye–Scherrer formula,^[34] showing that the size of the nanocrystals that build the NBs increase with increasing Gd amount, amounted to 21 nm for TiO₂ NBs, 30 nm for TiO₂@5%Gd NBs, and 42 nm for TiO₂@10%Gd NBs. A small amount of Gd doping (5 and 10 mol%) resulted in an increased crystalline size for anatase titania, while crystallinity decreased with high doping concentration (15 mol%). This variation in the anatase crystallite size with respect to Gd-doping can be rationalized regarding the ionic radii of the dopant and matrix. There are strong differences in the chemical properties of Gd³⁺ and Ti⁴⁺, and the mismatch in the ionic radii (180 ± 6 and 68 pm, respectively) makes it increasingly difficult to substitute Ti⁴⁺ by Gd³⁺ within the anatase lattice without perturbing the structure. Depending on the concentration, Gd³⁺ ions can then adopt different environments when incorporated within titania, where Gd is in low concentration will likely enter the titania lattice, which is the reason for the increased crystal size.^[36] It has also been reported that when the lanthanide content increases, most dopant cations will be incorporated close to the semiconductor crystallite surface in a glass-like environment, inhibiting the host material crystallization process.^[37]

For higher concentrations, sufficient Gd and oxygen content can then result in a beneficial environment for the creation of new crystalline phases with RE participation. In the highest concentrations adopted here, TiO₂@20%Gd, an outer crystalline structure is also formed (**Figure 3e**) that likely can be attributed to the new crystalline phase apparent in the XRD pattern for this sample (**Figure 2b**). In the XRD pattern of TiO₂@20%Gd NBs, the (105) and (213) peaks can be assigned to reflections from the anatase phase of TiO₂, while the predominant phase for this structure is the pyrochlores phase, with (004) and (102) peaks that can be assigned to Gd₂TiO₅, and peak (551) assigned to Gd₂Ti₂O₇ (JCPDS number: 21-1272).^[38,39] In both figures, peaks named FTO (fluorine-doped tin oxide conducting glass) are attributed to the sample substrate.

The Raman spectra of the TiO₂ NBs, TiO₂@5%Gd NBs, TiO₂@10%Gd NBs, and TiO₂@15%Gd NBs match with the anatase phase (**Figure 2c**).^[40] The anatase has six Raman active modes (A_{1g} + 2B_{1g} + 3E_g), which all appear in the Raman spectra of TiO₂ NBs and TiO₂@5%Gd NBs (**Figure 2c**). Among them, three E_g modes are centered around 144, 197, and 640 cm⁻¹ (designated E_{g1}, E_{g2}, and E_{g3}), and two B_{1g} modes located at 399 and 515 cm⁻¹ (designated

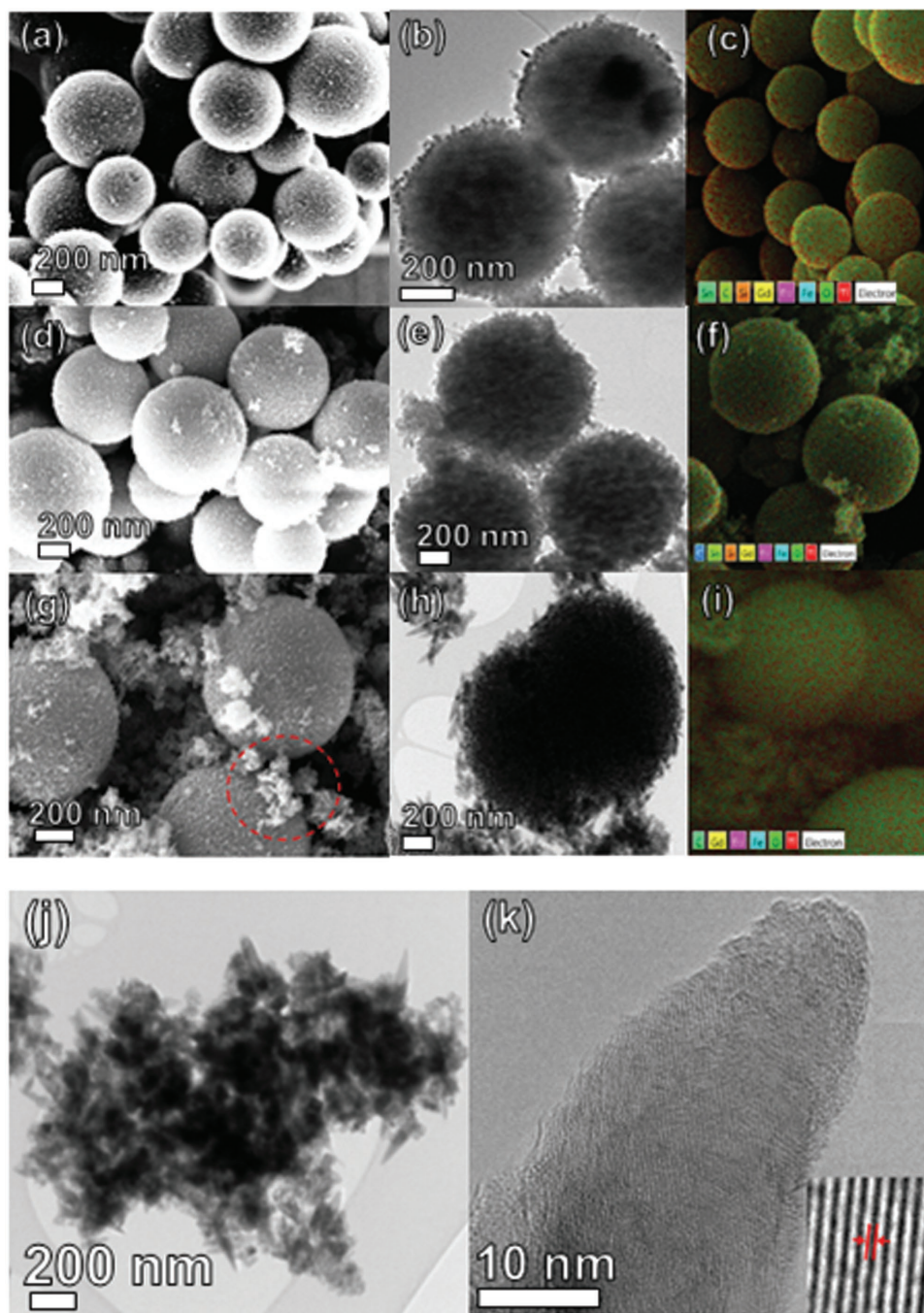


Figure 1. a,d,g) SEM, b,e,h) TEM, and c,f,i) EDS images of obtained structure: a–c) TiO_2 NBs, d–f) $\text{TiO}_2@5\%\text{Gd}$ NBs, and g–i) $\text{TiO}_2@10\%\text{Gd}$ NBs; red circle indicating the nanostar clusters in $\text{TiO}_2@10\%\text{Gd}$ NBs. j) TEM and k) HRTEM images of nanostar clusters, the crystalline plane of the nanoparticle is shown in (k).

$B_{1g(1)}$ and $B_{1g(2)}$).^[40] Because the peak positions of A_{1g} and $B_{1g(2)}$ are almost the same, we do not differentiate them here. The E_{g1} mode that corresponds to the symmetric lattice angular vibration is the strongest characteristic peak of anatase, as seen in Figure 2c. By increasing the Gd amount, the intensity of this mode decreased monotonically, in good agreement with decreased anatase crystallinity upon Gd doping.^[35] In the Raman spectrum of $\text{TiO}_2@20\%\text{Gd}$ NBs (Figure 2d), the Raman modes assigned to the anatase phase were not observed but instead showed Raman active modes

at 264 and 450 cm^{-1} characteristics of $\text{Gd}_2\text{Ti}_2\text{O}_7$,^[38,41] in very good agreement with XRD results.

2.2. Optical and Magnetic Resonance Imaging of $\text{TiO}_2@x\text{Gd}$ NBs

PL spectra show that the emission of Gd-doped TiO_2 spheres was dominated by a red emission peak at 636 nm upon UV excitation (Figure 3a), which previously has been assigned to

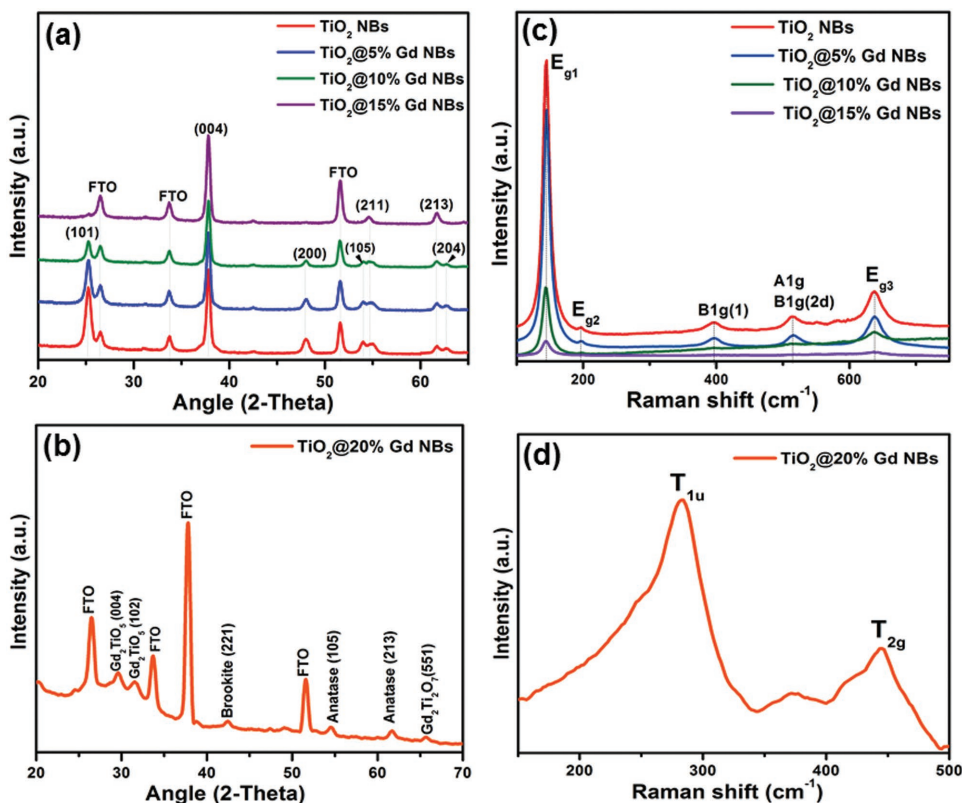


Figure 2. XRD spectra of synthesized structures: a) TiO_2 NBs, $\text{TiO}_2@5\% \text{Gd NBs}$, $\text{TiO}_2@10\% \text{Gd NBs}$, $\text{TiO}_2@15\% \text{Gd NBs}$, and b) $\text{TiO}_2@20\% \text{Gd NBs}$; Raman shift spectra of synthesized structures: c) TiO_2 NBs, $\text{TiO}_2@5\% \text{Gd NBs}$, $\text{TiO}_2@10\% \text{Gd NBs}$, and $\text{TiO}_2@15\% \text{Gd NBs}$, and d) $\text{TiO}_2@20\% \text{Gd NBs}$. Corresponding Raman-active modes are labeled in the figure.

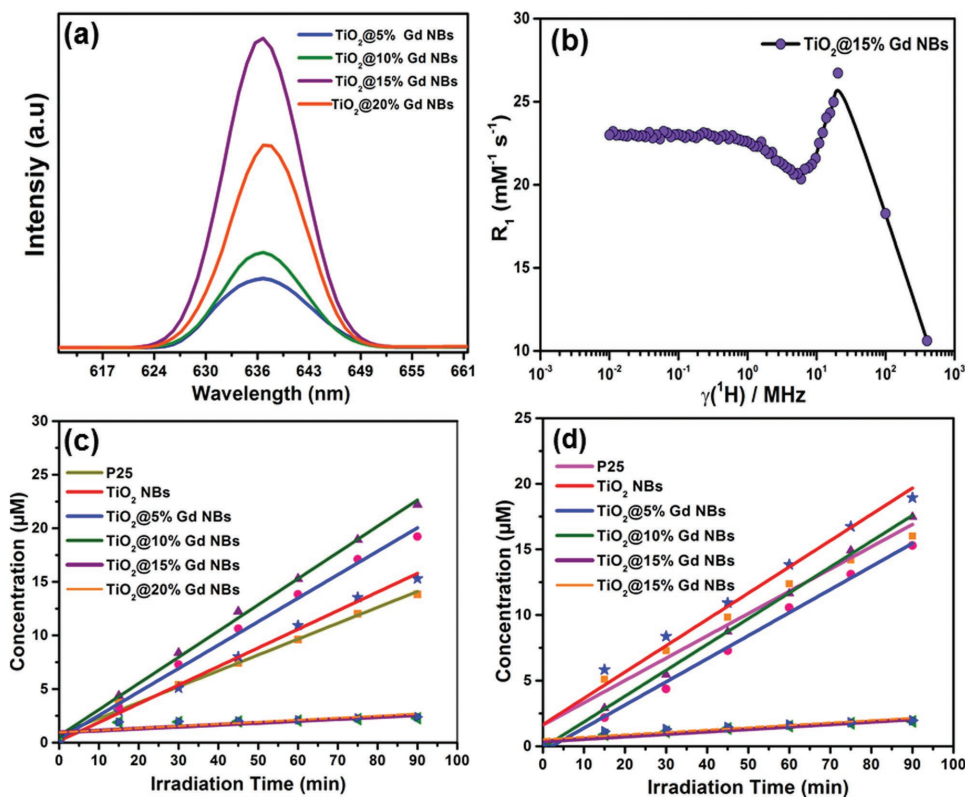


Figure 3. a) Room temperature photoluminescence spectra of Gd^{3+} -doped TiO_2 spheres upon UV (320 nm) excitation. b) ^1H NMRD profile for $\text{TiO}_2@15\% \text{Gd NBs}$ at 298 K. c,d) Dependence of resulting 7-hydroxycoumarin concentration to the irradiation time; c) in the absence of H_2O_2 , d) in the presence of H_2O_2 . Concentration was calculated from the fluorescence measurement of $0.1 \times 10^{-3} \text{ M}$ coumarin.

an atomic-like $f-f$ transition.^[29] In line with this, we observe an increasing emission intensity with increasing Gd amount, and the strongest emission was observed in the case of $\text{TiO}_2@15\%\text{Gd}$ NBs, which is attributed to the structure of the NBs. According to XRD, TEM, and the Raman results, we can conclude that the $\text{TiO}_2@15\%\text{Gd}$ NBs are primarily a mixture of anatase and amorphous phases. It has been suggested that the semi-crystalline TiO_2 structure is an excellent host for RE^{3+} ^[37] and here seen to show highest PL intensity for 15% Gd, while higher Gd content instead shows a $\text{Gd}_2\text{Ti}_2\text{O}_7$ structure from Raman and XRD. The rich spectral properties of certain RE ions, when incorporated in host materials, are highly attractive in many ways. However, RE ions alone are weakly fluorescent due to the parity forbidden $f-f$ transitions.^[51] Lanthanides possess a unique orbital arrangement resulting in a large Stoke's shift and a narrow emission and have therefore been a natural choice for imparting photoluminescence. TiO_2 lattices have proved to be an excellent host material for RE ions due to their good thermal, chemical, and mechanical stabilities.^[42] Titania nanocrystals surrounded by regions of amorphous titania have previously been proposed to act as effective light-harvesting antennae to absorb light and transfer energy to RE ions, which emit intense sharp luminescence,^[29,30] and also that a half-filled electronic configuration of RE dopant is beneficial for improving the photocatalytic activity of TiO_2 .^[43]

Paramagnetic gadolinium(III) ions (Gd^{3+}) possess seven unpaired electrons, which can efficiently alter the relaxation time of surrounding water protons, and have been widely used in routine clinical imaging as MRI contrast agents.^[21] To investigate how Gd^{3+} doped TiO_2 NBs would function as contrast agent in MRI, the relaxation times (T_1 , T_2) of $\text{TiO}_2@x\text{Gd}$ NBs were measured in a static magnetic field at 400 MHz (Table S1, Supporting Information). Both the spin–lattice relaxation time (T_1) and the spin–spin relaxation time (T_2) were shortened for Gd^{3+} doped TiO_2 NBs in comparison with pure TiO_2 NBs. However, relaxation rates $R_1 = 1/T_1$ and $R_2 = 1/T_2$ enhancements expressed as millimolar relaxivities r_1 and r_2 were significantly different for various samples where shape, size, crystallinity, and surface arrangement of the MRI contrast agent have a strong effect on longitudinal and transverse relaxation times.^[21] Based on the data presented in Table S1 (Supporting Information), there was no high T_1 shortening effect in the cases of $\text{TiO}_2@5\%\text{Gd}$ NBs, $\text{TiO}_2@10\%\text{Gd}$ NBs, and $\text{TiO}_2@20\%\text{Gd}$ NBs, while $\text{TiO}_2@15\%\text{Gd}$ NBs encountered a quite high T_1 shortening effect, with relaxivity being a few times greater than in commercial materials.^[44] The accessibility of water to Gd^{3+} ions is the main factor in the shortening of T_1 . It has previously been suggested that a rigid crystal lattice could greatly reduce the Gd^{3+} ions' water accessibility, resulting in a limited contribution to T_1 shortening.^[45] The XRD and Raman results are presented above confirmed that $\text{TiO}_2@5\%\text{Gd}$ NBs and $\text{TiO}_2@10\%\text{Gd}$ NBs are well crystallized structures and therefore have limited contribution to T_1 shortening; however, the $\text{TiO}_2@15\%\text{Gd}$ NBs here show a retained anatase structure from Raman and partly amorphous character from the broad background in XRD and TEM images, thus $\text{TiO}_2@15\%\text{Gd}$ NBs seem to be around the

optimum composition for delivering the best MRI response as well as PL intensity.

Data in Table S1 of the Supporting Information show the same trend as T_1 was the shortest; T_2 relaxation time was found for $\text{TiO}_2@15\%\text{Gd}$ MBs. T_2 is related to the magnetic moment of the imaging contrast agents and thereby to their size. The magnetic moment of nanoparticles rapidly decreases as their sizes decrease due to the reduction in the volume magnetic anisotropy and spin disorders on the surface of the nanoparticles.^[46] In general, controlling the size of nanoparticles is critical for achieving a strong $R_2 = 1/T_2$ enhancement, where the theoretically predicted maximum of r_2 relaxivity can be approached by optimizing the overall size of contrast agent.^[46] The relaxivity recorded for the $\text{TiO}_2@15\%\text{Gd}$ NBs was surprisingly high ($r_2 = 126 \text{ mm}^{-1} \text{ s}^{-1}$) compared to a commonly available contrast agent for T_2 shortening,^[21] and could thus be promising for use as efficient MRI contrast agent. An NMRD measurement was conducted for this sample to obtain more information about its MRI function. The field dependence of the proton relaxation rate for (NMRD profile) $\text{TiO}_2@15\%\text{Gd}$ NBs is shown in Figure 3b. As expected, the undoped TiO_2 NBs show a flat NMR profile (not shown in the figure) while the 15% Gd-doped TiO_2 relaxivity is strongly increased and resembles a typical NMRD profile of the MRI contrast agents,^[47] with highest relaxivity $r_1 = 27 \text{ mm}^{-1} \text{ s}^{-1}$ at 20 MHz. It has been previously reported that densely packed nanoparticles have high magnetizations, and it is likely that the high relaxivities of $\text{TiO}_2@15\%\text{Gd}$ NBs also here can be attributed to the packing of the local structure, i.e., densely packed nanoparticles in cluster form as observed from Figure S1b of the Supporting Information.

2.3. Photocatalytic Activity of $\text{TiO}_2@x\text{Gd}$ NBs

To evaluate cancer cell destruction capability (based on ROS photogeneration) of synthesized structures, the photocatalytic activities of synthesized structures were quantified using a fluorescence probe method with coumarin, which is regarded as a viable indirect detection method for the presence of hydroxyl radicals.^[48] $\cdot\text{OH}$ is an extremely important species, being frequently assigned as the major reactant responsible for the photocatalytic oxidation of organic compounds and deactivation of microorganisms.^[49] The formation of $\cdot\text{OH}$ radicals on the synthesized structure surface was probed by measuring the fluorescence intensity of 7-hydroxycoumarin that is formed upon the reaction of coumarin with $\cdot\text{OH}$ radicals.^[50] Figure 3a shows the amount of 7-hydroxycoumarin, produced by different synthesized structures under irradiation with UV-A, as a function of the irradiation time. Moreover, the effect of H_2O_2 on the formation of $\cdot\text{OH}$ radicals was investigated, and the result was presented in Figure 3b. Linear increases in the concentration of 7-hydroxycoumarin were observed as a function of the UV-A illumination time for all experiments (Figure 3a,b) where the $\cdot\text{OH}$ generation rate (r), without and with H_2O_2 , was calculated from the slope of the lines^[51] (Table 1). A common parameter to determine and compare photocatalytic activities is the photonic efficiency (ζ) for which the $\cdot\text{OH}$ generation is calculated

Table 1. $\cdot\text{OH}$ generation rates: photonic efficiencies of $\cdot\text{OH}$ generation under irradiation with UV-A for different photocatalysts.

	Rate of $\cdot\text{OH}$ generation without H_2O_2 ($\mu\text{M min}^{-1}$)	Photonic efficiency % without H_2O_2	Rate of $\cdot\text{OH}$ generation with H_2O_2 ($\mu\text{M min}^{-1}$)	Photonic efficiency % with H_2O_2
P25	0.148	0.820	0.170	0.940
TiO_2 NBs	0.174	0.963	0.200	1.109
$\text{TiO}_2@5\%\text{Gd}$ NBs	0.219	1.211	0.176	0.974
$\text{TiO}_2@10\%\text{Gd}$ NBs	0.245	1.353	0.197	1.089
$\text{TiO}_2@15\%\text{Gd}$ NBs	0.005	0.029	0.011	0.061
$\text{TiO}_2@20\%\text{Gd}$ NBs	0.007	0.037	0.014	0.076

from the rate of $\cdot\text{OH}$ generation (r) divided by the incident photon flux (I_0), according to the following equation^[52,53]

$$(\zeta)^{\frac{1}{2}} r100 = I_0 \quad (1)$$

The photonic efficiencies of $\cdot\text{OH}$ generation, without and with H_2O_2 , are summarized in Table 1.

The results show that in the absence of H_2O_2 the photonic efficiencies of $\cdot\text{OH}$ generation with $\text{TiO}_2@5\%\text{Gd}$ NBs and $\text{TiO}_2@10\%\text{Gd}$ NBs are significantly higher than TiO_2 NBs and P25.^[53] Presence of 0.1×10^{-3} M H_2O_2 had a contradictory effect on the formation of $\cdot\text{OH}$ on the different nanobeads, where the addition of 0.1×10^{-3} M H_2O_2 led to a significant increase of photonic efficiencies of $\cdot\text{OH}$ generation with P25 and pure TiO_2 NBs.^[50] On the other hand, for $\text{TiO}_2@5\%\text{Gd}$ NBs and $\text{TiO}_2@10\%\text{Gd}$ NBs, adding 0.1×10^{-3} M H_2O_2 had a negative effect. In the absence as well presence of H_2O_2 , photonic efficiencies of $\cdot\text{OH}$ generation with $\text{TiO}_2@15\%\text{Gd}$ NBs and $\text{TiO}_2@20\%\text{Gd}$ NBs were negligible compared to other structures. From the results it is clear that low concentrations

of Gd (5%–10% Gd) are beneficial for ROS generation in the photocatalytic activity of TiO_2 NBs, with a maximum ROS photogeneration for 10% Gd doping, while the higher concentrations of 15% and 20% Gd lead to much lower anatase crystallinity^[54] and reduce the ROS photogeneration dramatically (Table 1 and Figure 3). The enhancement of photocatalytic activity after Gd-doping can be assigned to the higher adsorption, improved charge-transfer efficiency, and the prevention of electron–hole recombination.^[1] To further explore how the electronic changes in the Gd-doped TiO_2 affect the absorption and possibly improved charge transfer and electron–hole recombination, DFT calculations were performed and analyzed for undoped and Gd-doped anatase TiO_2 .^[36,55]

2.4. DFT Calculations

Corresponding unit cells of undoped and Gd-doped TiO_2 anatase are depicted in **Figure 4a,d**. In the case of doping, the

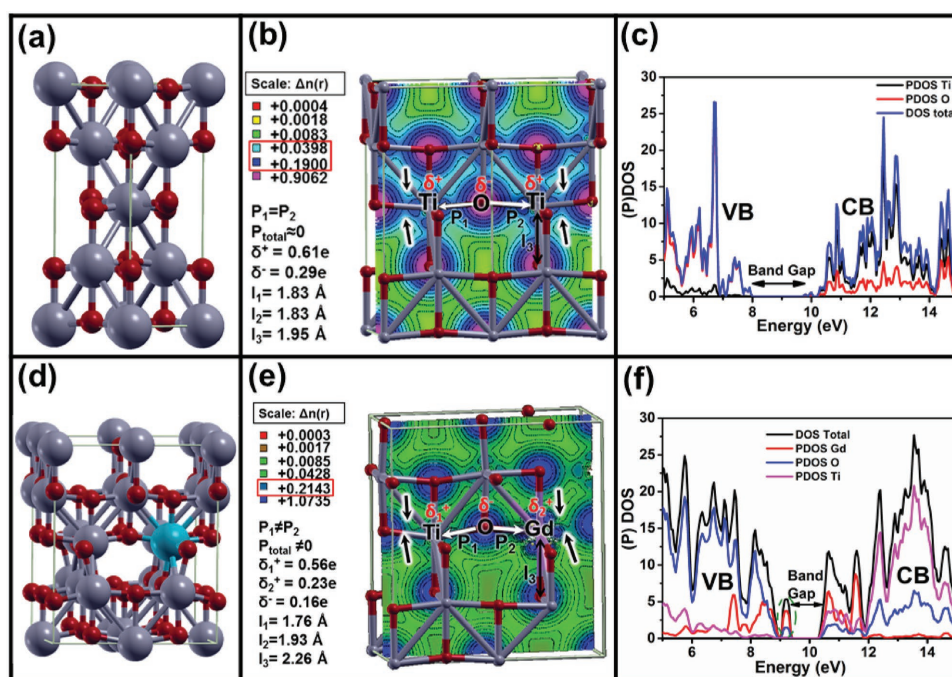


Figure 4. a) Unit cell, b) charge density distribution, c) PDOS of anatase TiO_2 . d) Unit cell, e) charge density distribution, f) PDOS of 12% Gd-doped anatase TiO_2 .

replacement of Ti with Gd within the anatase lattice is accompanied by structural changes, due to a different cation radius and charge of Gd that further affect ground-state charge density distribution and the density of states (DOS).^[56] Figure 4 compares the charge density distribution within the lattice of anatase and Gd-doped anatase (Figure 4b,e), and also the corresponding calculated DOS and partial DOS (PDOS) (Figure 4c,f). By considering the atoms in the lattice as charged ions, Löwdin charge analysis can be used for estimation of the dipole moments in the lattice,^[57] providing the relative magnitudes and directions of the dipoles in the doped and undoped lattices. Regarding the data presented in Figure 4, the in-plane dipole moment for the TiO₂ lattice was zero (due to the symmetry illustrated in Figure 4b); however, for the Gd-doped TiO₂ it was estimated to be 1.1 Debye (Figure 4e).

The comparison of our calculated PDOS and total DOS of anatase TiO₂ and Gd-doped anatase TiO₂ (Figure 4c,f) reveals that the Gd³⁺ ions introduced impurity energy levels (IELs) inside the bandgap (at the top of valence band), and that, consequently, the bandgap is slightly narrowed by Gd doping. IELs inside the bandgap of anatase TiO₂ consist of RE 4f states, RE 5d states, and RE 6s² states, which influence the positions, widths, and DOS of CB and VB of anatase TiO₂, consistent with previous work with RE in TiO₂.^[55]

The full photocatalysis reaction is a complicated process, including light absorption, excitation, and migration of photo-excited charge carriers, redox reaction on the surface with possible chemical species interaction and surface reconstructions, as well as mass transport limitations and back reactions.^[1] Some parts of this reaction, such as the charge separation efficiency, charge transfer, and charge recombination at the TiO₂ surface, can be affected by Gd-doping.^[58] The presence of Gd induces some structural changes in the unit cell by distorting the metal-oxide octahedron bond lengths and angles (summarized in Table S2 of the Supporting Information for the case of 12% doping as examples). The changes in cell volume, bond length, and charge on atoms result that the center of gravity of negative electric charges deviates from the position of the Ti⁴⁺ ion in the TiO₆ octahedron, and its dipole moment is consequently no longer zero.^[57] Charge imbalance and local permanent dipoles would facilitate more efficient charge separation upon excitation and subsequent charge transport, but it may also help OH adsorption on the surface and retard the recombination,^[1] and consequently enhance the ROS photogeneration. In addition to nonzero dipole moment induced by doping (as depicted in Figure 4d by white arrows), after doping, the distribution of charge density along the covalent bond of metal–oxygen is enhanced. This is in agreement with the calculated Löwdin charge of the atoms (presented in Table S2 of the Supporting Information) and shows less ionic and more covalent nature of the bonds that can facilitate the charge transport from the bulk to the surface of the particle.^[59]

2.5. Biocompatibility of TiO₂@xGd NBs and Photocatalytic Treatments of Cancer Cells: In Vitro Study

The relatively low ROS photogeneration activity of the TiO₂@15%Gd and TiO₂@20%Gd NBs would make them less

promising candidates for single use in PDT, but instead very promising for MRI contrast. Application of TiO₂@xGd NBs in PDT with simultaneous therapeutic and imaging efficacies is desirable for the future,^[16] and therefore TiO₂ NBs doped with high concentration were neglected, and just TiO₂ NBs, TiO₂@5%Gd NBs, and TiO₂@10% Gd NBs were considered for in vitro studies.

Cytotoxicity of TiO₂@xGd NBs was tested by Resazurin assay and the results presented in the Figure S10 of the Supporting Information. The cytotoxicity results (Figure S10, Supporting Information) show that viability of the cell was not affected by TiO₂@xGd NBs for all tested concentrations (10, 50, 75, 100, 200 µg mL⁻¹) and TiO₂@xGd NBs fully biocompatible. There is a reverse relation between biocompatibility and size of nanostructures; smaller nanostructures with a higher surface area are more active for ROS generation, however they show more cytotoxicity. Engineered TiO₂@xGd NBs avoid cytotoxicity, having a size greater than 100 nm; while, on the other hand, TiO₂@xGd NBs, keeping high surface area and mesoporosity, have a high capacity for ROS photogeneration. Morphological alteration of MG-63 cells treated with different TiO₂@xGd NBs was monitored with light and differential interference contrast (DIC) microscopy. Microscopy images (Figure 5b–d) proved that the morphology of MG-63 cells treated with TiO₂@xGd NBs did not differ from the morphology of untreated control cells (Figure 5a), which could be explained as high biocompatibility. The most significant finding of our work is cellular internalization of TiO₂@xGd NBs (Figure 5b–d), which is much more significant in the case of TiO₂@10%Gd NBs compared to the TiO₂@5%Gd NBs or undoped TiO₂ NBs, although all cells were treated with the same TiO₂@xGd NBs concentration (50 µg mL⁻¹). We noticed that the majority of TiO₂@xGd NBs were located around the cell nuclei (Figure 5b–d). More experiments were done to examine acid organelles after cellular treatment with TiO₂@xGd NBs. Cells treated with 50 µg mL⁻¹ of TiO₂@xGd NBs and incubated for 24 h had enlarged acid organelles and compared to untreated control cells (Figure 5e–g). We speculate that enlarged acid organelles are filled with NBs, indicating that MG-63 human cancer cells endocytose NBs.^[60–62] The flat/spread appearance of the cells gives room for cellular inclusions only around the nucleus in a dome-shaped central part of the cell. TEM analysis was performed to confirm the internalization of NBs. Figure S11 of the Supporting Information shows a perinuclear region with TiO₂@10%Gd NBs inclusions.

Since MG-63 human cancer cells endocytose TiO₂@xGd NBs, they could concentrate TiO₂@xGd NBs and this can significantly improve specificity for imaging and damage cancerous cells, together with low systemic toxicity.^[63] MG-63 cells incubated with TiO₂@xGd NBs were irradiated with an LED lamp for a different period (3, 4, 5 min) to specific photocatalytic ROS generation inside of MG-63 cells. Upon irradiation, the excited TiO₂@xGd NBs transfer energy to the surrounding O₂ and H₂O to generate ROS, which can be exploited to destroy cancer cells.^[5] The produced ROS exhibits an extremely short lifespan and severely limited diffusion distance, so the damage of ROS to biomolecules

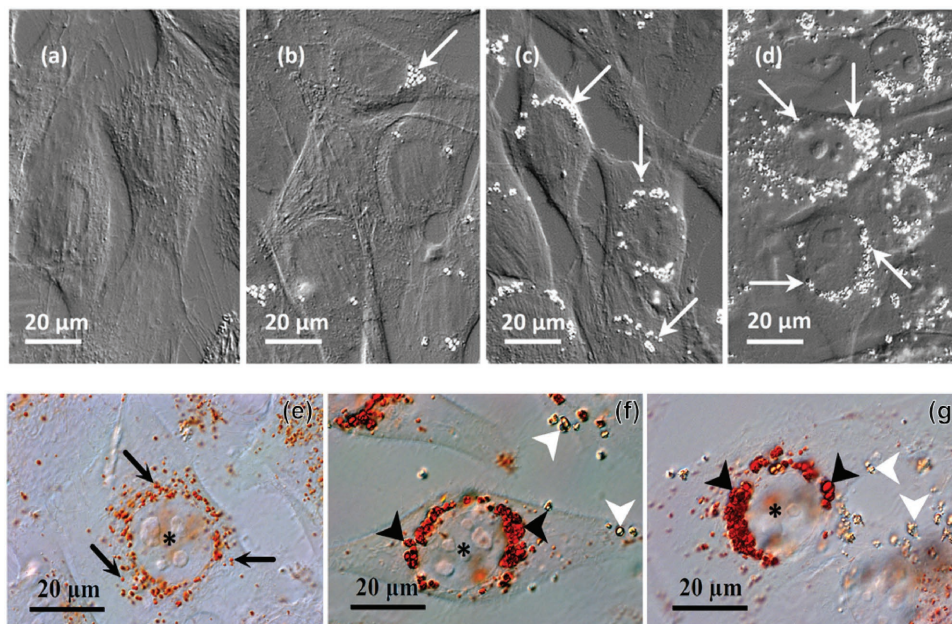


Figure 5. a–d) MG-63 cells treated with $\text{TiO}_2@x\text{Gd}$ NBs. Differential interference contrast (DIC) images of MG63 cells after 1 h incubation with $50 \mu\text{g mL}^{-1}$ NBs: a) untreated control cells; b) cells treated with TiO_2 NBs; c) cells treated with $\text{TiO}_2@5\%\text{Gd}$ NBs; d) cells treated with $\text{TiO}_2@10\%\text{Gd}$ NBs; arrows are showing NBs. e–g) Acid organelles in MG-63 cells treated with $\text{TiO}_2@x\text{Gd}$ NBs. DIC images of MG-63 cells after 1 h incubation with $50 \mu\text{g mL}^{-1}$ NBs and additional 24 h incubation. Acid organelles are stained red by neutral red dye. In untreated control cell (e) acid organelles are the small and round shape (arrows). In f) $\text{TiO}_2@5\%\text{Gd}$ NBs and g) $\text{TiO}_2@10\%\text{Gd}$ NBs treated cell, acid organelles are bigger and irregular shape (black arrowheads). The shape of red acid organelles is similar to uninternalized, unstained NBs (white arrowheads). Cell nuclei are marked with an asterisk.

is strongly restricted to the immediate vicinity of ROS photogeneration.^[11] Mitochondria are the primary source of cellular ROS generation (approximately up to 90%), and mitochondrial dysfunctions are closely correlated with the disruption in the balance of mitochondrial ROS. Also, mitochondria are decisive regulators of the intrinsic pathway of apoptosis, which is regarded as the major mode of cell death in cancer therapy.^[64,65] Resazurin assay is an extremely sensitive, simple, and nontoxic procedure to evaluate mitochondrial function.^[66] After photocatalytic treatment, the controlled manipulation of mitochondrial activity was further estimated with resazurin assay.

Resazurin assay result after photocatalytic treatment showed that survival rate of MG-63 cancer cells depends on irradiation time, and for irradiation longer than 4 min cell population in a control group suffers from UV-A irradiation (**Figure 6**). However, after 3 min irradiation, the cell viability in the control group was more than 90%, suggesting 3 min UV-A irradiation possessed good biocompatibility. For certain irradiation times, cells pretreated with $\text{TiO}_2@x\text{Gd}$ NBs were more vulnerable to UV-A irradiation; this means $\text{TiO}_2@x\text{Gd}$ NBs deliver their photocatalytic activity and ROS photogeneration potential for cancer cells destruction. After 3 min of UV-A irradiation, $\text{TiO}_2@10\%\text{Gd}$ NBs showed enhanced photocatalytic activity compared to undoped TiO_2 NBs and $\text{TiO}_2@5\%\text{Gd}$ NBs for cancer cells destruction, in good agreement with our other experiments and theoretical calculation.

3. Conclusion

The current study presents the synthesis, characterization, and performance of novel biocompatible and multifunctional Gd-doped TiO_2 in the sub-micrometer range, intended with a potential for cancer cells tracking and killing. Our results showed that the ROS photogeneration capacity of the TiO_2 NBs doped with a low concentration of Gd (5% Gd and 10% Gd) was increased compared to TiO_2 NBs and P25. ROS photogeneration capacity of those TiO_2 NBs doped with high concentration of Gd (15% and 20% Gd) significantly decreased in comparison with undoped TiO_2 NBs and P25, while instead providing better OI and MRI contrast effect, especially for $\text{TiO}_2@15\%\text{Gd}$ NBs. According to our result, we suggested $\text{TiO}_2@10\%\text{Gd}$ NBs as a promising candidate with high ROS photogeneration capacity and increased OI and MRI effect. T_1 shortening effect of $\text{TiO}_2@10\%$ Gd NBs was moderate ($r_1 = 4.7 \text{ mm}^{-1} \text{ s}^{-1}$); however, T_2 shortening effect of this sample was high ($r_2 = 80 \text{ mm}^{-1} \text{ s}^{-1}$), where r_2 relaxivity of $\text{TiO}_2@10\%\text{Gd}$ NBs was even a few times more than clinically available contrast agent.^[67] However, if target is only the imaging capabilities, the $\text{TiO}_2@15\%\text{Gd}$ NBs showed the largest PL intensity, as well as strong relaxation rate $1/T_2$, where r_2 was $126 \text{ mm}^{-1} \text{ s}^{-1}$. In vitro cytotoxicity of $\text{TiO}_2@x\text{Gd}$ NBs tested by measuring mitochondrial activity associated with viability assay and the results confirmed that $\text{TiO}_2@x\text{Gd}$ NBs are fully biocompatible for all tested concentration. Regarding ROS photogeneration capacity of $\text{TiO}_2@x\text{Gd}$ NBs, in agreement with

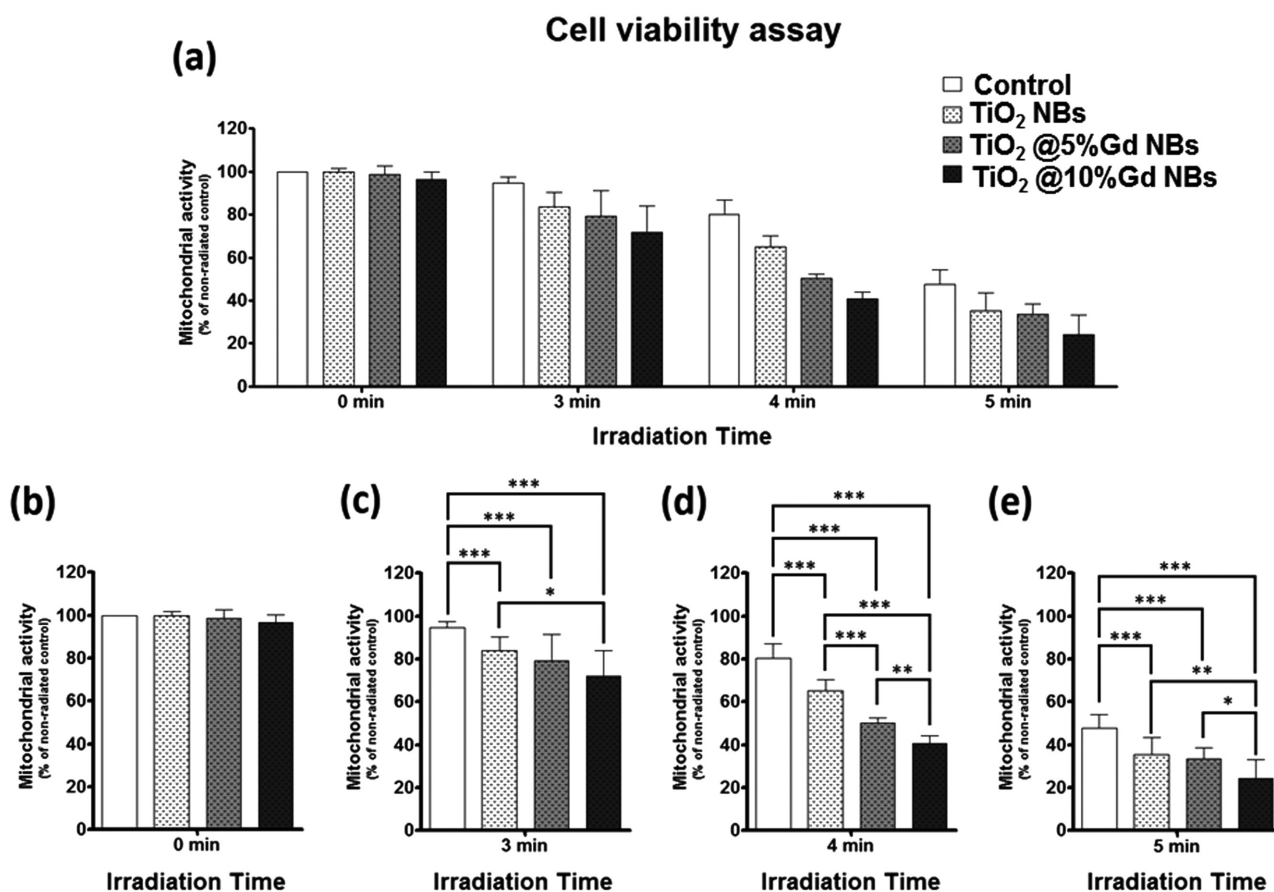


Figure 6. a) Cell viability of MG-63 cells after 1 h exposure to TiO₂@xGd NBs followed by UV-A radiation and 24 h postincubation, tested by resazurin assay. Results are presented as the mean (+SD) percentage of untreated, nonirradiated control in the experiment performed twice in at least five replica wells. b–e) Asterisks in the lower graphs denote the significant differences between samples (**p* < 0.05; ***p* < 0.01; ****p* < 0.001; Student's *t*-test). Cell viability between nonirradiated samples (0 min) treated with TiO₂(+ Gd) NBs did not significantly differ in comparison to untreated control.

results obtained with our other experiments and theoretical calculation, TiO₂@10%Gd NBs showed highest photocatalytic activity already after 3 min of irradiation with UV-A.

To the end, since TiO₂@xGd NBs produce ROS only when they are photoactivated, they form a fully biocompatible system for MRI and up to 3 min of irradiation in combined PDT treatment and OI-MRI, and would form a promising platform for simultaneous cancer cell imaging and treatment by PDT.

(ARRS) grants J1-6728 and P2-0232 for the financial support in carrying out this research. The authors would like to thank Dr. Leif Häggman in Uppsala University for support in the SEM and EDAX measurements, Prof. Igor Serša in Jozef Stefan Institute for his handfull help MRI measurements, and Prof. Andreja Erman in Cell Biology Institute, Slovenia, for her assistance in TEM imaging of cells. The authors acknowledge Uppsala Multidisciplinary Centre for Advanced Computational Science (UPPMAX) for providing the computational resources under Projects snic2015-6-65.

Supporting Information

Supporting Information is available from the Wiley Online Library or from the author.

Acknowledgements

M.P., T.A., V.K., and N.R. contributed equally to this work. The authors wish to acknowledge the Slovenian Research Agency

- [1] J. Schneider, M. Matsuoka, M. Takeuchi, J. Zhang, Y. Horiuchi, M. Anpo, D. W. Bahnemann, *Chem. Rev.* **2014**, *114*, 9919.
- [2] T. Rajh, N. M. Dimitrijevic, M. Bissonnette, T. Koritarov, V. Konda, *Chem. Rev.* **2014**, *114*, 10177.
- [3] Z. F. Yin, L. Wu, H. G. Yang, Y. H. Su, *Phys. Chem. Chem. Phys.* **2013**, *15*, 4844.
- [4] Z. Hu, Y. Huang, S. Sun, W. Guan, Y. Yao, P. Tang, C. Li, *Carbon* **2012**, *50*, 994.
- [5] H. K. Patra, R. Imani, J. R. Jangamreddy, M. Pazoki, A. Iglíč, A. P. F. Turner, A. Tiwari, *Nat. Sci. Rep.* **2015**, *5*, 14571.
- [6] M. Song, R. Zhang, Y. Dai, F. Gao, H. Chi, G. Lv, B. Chen, X. Wang, *Biomaterials* **2006**, *27*, 4230.
- [7] M. Xu, N. Huang, Z. Xiao, Z. Lu, *Supramol. Sci.* **1998**, *5*, 449.

- [8] J. W. Seo, H. Chung, M. Y. Kim, J. Lee, I. H. Choi, J. Cheon, *Small* **2007**, *3*, 850.
- [9] J. Petković, T. Küzma, K. Rade, S. Novak, M. Filipič, *J. Hazard. Mater.* **2011**, *196*, 145.
- [10] a) T. Tachikawa, M. Fujitsuka, T. Majima, *J. Phys. Chem. C* **2007**, *111*, 5259; b) D. M. Blake, P.-C. Maness, Z. Huang, E. J. Wolfrum, J. Huang, W. A. Jacoby, *Sep. Purif. Methods* **1999**, *28*, 1.
- [11] D. Trachootham, J. Alexandre, P. Huang, *Nat. Rev. Drug Discovery* **2009**, *8*, 579.
- [12] S. O. Gollnick, B. Owczarczak, P. Maier, *Nat. Rev. Cancer* **2006**, *6*, 535.
- [13] D. E. Dolmans, D. Fukumura, R. K. Jain, *Nat. Rev. Cancer* **2003**, *3*, 380.
- [14] S. Wu, Z. Weng, X. Liu, K. W. K. Yeung, P. K. Chu, *Adv. Funct. Mater.* **2014**, *24*, 5464.
- [15] H. Peng, X. Liu, G. Wang, M. Li, K. M. Bratlie, E. Cochran, Q. Wang, *J. Mater. Chem. B* **2015**, *3*, 6856.
- [16] M. Li, H. Deng, H. Peng, Q. Wang, *J. Nanosci. Nanotechnol.* **2014**, *14*, 415.
- [17] F. Jia, X. Liu, L. Li, S. Mallapragada, B. Narasimhan, Q. Wang, *J. Controlled Release* **2013**, *172*, 1020.
- [18] F. Wang, W. B. Tan, Y. Zhang, X. Fan, M. Wang, *Nanotechnology* **2006**, *17*, R1.
- [19] M. H. Li, H. Yu, T. F. Wang, N. D. Chang, J. Q. Zhang, D. Du, M. F. Liu, S. L. Sun, R. Wang, H. Q. Tao, S. L. Geng, Z. Y. Shen, Q. Wang, H. S. Peng, *J. Mater. Chem. B* **2014**, *2*, 1619.
- [20] D. Du, N. Chang, S. Sun, M. Li, H. Yu, M. Liu, X. Liu, G. Wang, H. Li, X. Liu, S. Geng, Q. Wang, H. Peng, *J. Controlled Release* **2014**, *182*, 99.
- [21] H. Bin Na, I. C. Song, T. Hyeon, *Adv. Mater.* **2009**, *21*, 2133.
- [22] M. S. Eljamel, *Photodiagn. Photodyn. Ther.* **2008**, *5*, 260.
- [23] J. Cao, R. Wang, N. Gao, M. Li, X. Tian, W. Yang, Y. Ruan, C. Zhou, G. Wang, X. Liu, S. Tang, Y. Yu, Y. Liu, G. Sun, H. Peng, Q. Wang, *Biomater. Sci.* **2015**, *3*, 1545.
- [24] H. Dong, G. Zeng, L. Tang, C. Fan, C. Zhang, X. He, Y. He, *Water Res.* **2015**, *79*, 128.
- [25] M. C. Heffern, L. M. Matosziuk, T. J. Meade, *Chem. Rev.* **2014**, *114*, 4496.
- [26] Y. L. H. Liu, L. Yu, W. Chen, *J. Nanomater.* **2012**, *13*, 1.
- [27] M. Luo, K. Cheng, W. Weng, C. Song, P. Du, G. Shen, G. Xu, G. Han, *Nanoscale Res. Lett.* **2009**, *4*, 809.
- [28] W. Luo, C. Fu, R. Li, Y. Liu, H. Zhu, X. Chen, *Small* **2011**, *7*, 3046.
- [29] X. Chen, W. Luo, *J. Nanosci. Nanotechnol.* **2010**, *10*, 1482.
- [30] S. Sandoval, J. Yang, J. G. Alfaro, A. Liberman, M. Makale, C. E. Chiang, I. K. Schuller, A. C. Kummel, W. C. Troglter, *Chem. Mater.* **2012**, *24*, 4222.
- [31] A. D. Maynard, *Nature* **2011**, *475*, 31.
- [32] R. Imani, P. Veranic, A. Iglíc, M. E. Kreft, M. Pazoki, S. Hudoklin, *Photochem. Photobiol. Sci.* **2015**, *14*, 583.
- [33] R. Imani, M. Pazoki, A. Tiwari, G. Boschloo, A. P. F. Turner, V. Kralj-Iglič, A. Iglíc, *Nanoscale* **2015**, *7*, 10438.
- [34] R. Imani, A. Iglíc, A. P. F. Turner, A. Tiwari, *Electrochem. Commun.* **2014**, *40*, 84.
- [35] M. Pał, U. Pał, J. M. G. Y. Jiménez, F. Pérez-Rodríguez, *Nanoscale Res. Lett.* **2012**, *7*, 1.
- [36] P. Sudhagar, A. Devadoss, K. Nakata, C. Terashima, A. Fujishima, *J. Electrochem. Soc.* **2014**, *162*, H108.
- [37] V. S. Smitha, S. Pillai, U. N. S. Hareesh, B. N. Nair, K. G. Warriar, *RSC Adv.* **2014**, *4*, 61727.
- [38] N. J. Hess, B. D. Begg, S. D. Conradson, D. E. Mccready, P. L. Gassman, W. J. Weber, *J. Phys. Chem. B* **2002**, *106*, 4663.
- [39] A. Gómez-Pérez, J. Prado-Gonjal, D. Muñoz-Gil, A. Andrada-Chacón, J. Sánchez-Benítez, E. Morán, M. T. Azcondo, U. Amador, R. Schmidt, *RSC Adv.* **2015**, *5*, 85229.
- [40] C.-H. Yang, Z.-Q. Ma, *Appl. Opt.* **2012**, *51*, 5438.
- [41] J. Zhang, J. Lian, F. Zhang, J. Wang, A. F. Fuentes, R. C. Ewing, *J. Phys. Chem. C* **2010**, *2*, 11810.
- [42] H. Maas, A. Currao, G. Calzaferri, *Angew. Chem., Int. Ed.* **2011**, *41*, 2495.
- [43] J. Li, X. Yang, X. Yu, L. Xu, W. Kang, W. Yan, H. Gao, Z. Liu, Y. Guo, *Appl. Surf. Sci.* **2009**, *255*, 3731.
- [44] C. S. Info, *The Basic Textbook of the European Magnetic Resonance Forum*, 9th ed. European Magnetic Resonance Forum, e-book, **2016**.
- [45] F. Chen, W. Bu, S. Zhang, X. Liu, J. Liu, H. Xing, Q. Xiao, L. Zhou, W. Peng, L. Wang, J. Shi, *Adv. Funct. Mater.* **2011**, *21*, 4285.
- [46] E. Pösel, H. Kloust, U. Tromsdorf, M. Janschel, C. Hahn, C. Maßlo, H. Weller, *ACS Nano* **2012**, *6*, 1619.
- [47] L. Moriggi, C. Cannizzo, E. Dumas, C. R. Mayer, A. Ulianov, L. Helm, *J. Am. Chem. Soc.* **2009**, *131*, 10828.
- [48] C. Baumanis, J. Z. Bloh, R. Dillert, D. W. Bahnemann, *J. Phys. Chem. C* **2011**, *115*, 25442.
- [49] N. Wu, J. Wang, D. N. Tafen, H. Wang, J. G. Zheng, J. P. Lewis, X. Liu, S. S. Leonard, A. Manivannan, *J. Am. Chem. Soc.* **2010**, *132*, 6679.
- [50] J. Zhang, Y. Nosaka, *J. Phys. Chem. C* **2013**, *117*, 1383.
- [51] H. Kisch, D. Bahnemann, *J. Phys. Chem. Lett.* **2015**, *6*, 1907.
- [52] C. Wang, J. Rabani, D. W. Bahnemann, J. K. Dohrmann, *J. Photochem. Photobiol. A Chem.* **2002**, *148*, 169.
- [53] H. Zhang, D. W. Bahnemann, *J. Mater. Chem.* **2009**, *19*, 5089.
- [54] J. Z. Bloh, R. Dillert, D. W. Bahnemann, *J. Phys. Chem. C* **2012**, *116*, 25558.
- [55] L. Bian, M. Song, T. Zhou, X. Zhao, Q. Dai, *J. Rare Earths* **2009**, *27*, 461.
- [56] J. Choi, P. Sudhagar, P. Lakshminathiraj, J. W. Lee, A. Devadoss, S. Lee, T. Song, S. Hong, S. Eito, C. Terashima, T. H. Han, J. K. Kang, A. Fujishima, Y. S. Kang, U. Paik, *RSC Adv.* **2014**, *4*, 11750.
- [57] Z. Zhao, Q. Liu, *J. Phys. D: Appl. Phys.* **2008**, *41*, 085417.
- [58] S. Bingham, W. A. Daoud, *J. Mater. Chem.* **2011**, *21*, 2041.
- [59] A. V. Akimov, A. J. Neukirch, O. V. Prezhdo, *Chem. Rev.* **2013**, *113*, 4496.
- [60] L. M. Bareford, P. W. Swaan, *Adv. Drug Delivery Rev.* **2007**, *59*, 748.
- [61] Q. Wang, H. Cheng, H. Peng, H. Zhou, P. Y. Li, R. Langer, *Adv. Drug Delivery Rev.* **2015**, *91*, 125.
- [62] H. Peng, C. Wang, X. Xu, C. Yu, Q. Wang, *Nanoscale* **2015**, *7*, 4354.
- [63] Y. Mosesson, G. B. Mills, Y. Yarden, *Nat. Rev. Cancer* **2008**, *8*, 835.
- [64] Z. Yu, Q. Sun, W. Pan, N. Li, B. Tang, *ACS Nano* **2015**, *16*, 11064.
- [65] Z. Hou, Y. Zhang, K. Deng, Y. Chen, X. Li, X. Deng, Z. Cheng, H. Lian, C. Li, J. Lin, *ACS Nano* **2015**, *9*, 2584.
- [66] K. K. Abu-Amero, T. M. Bosley, *Arch. Pathol. Lab. Med.* **2005**, *129*, 1295.
- [67] A. Gizzatov, V. Keshishian, A. Guven, A. M. Dimiev, F. Qu, R. Muthupillai, P. Decuzzi, R. G. Bryant, J. M. Tour, L. J. Wilson, *Nanoscale* **2014**, *6*, 3059.

Received: January 31, 2017
Published online: